

Particle-like topologies of light in turbulent complex media

Danilo Gomes Pires,^{1,*} Vasilios Cocotos,^{2,*} Cade Peters,² Natalia M. Litchinitser,^{1,†} and Andrew Forbes^{2,‡}

¹*Department of Electrical and Computer Engineering, Duke University, Durham, USA*

²*School of Physics, University of the Witwatersrand, Private Bag 3, Wits 2050, South Africa*

(Dated: February 25, 2026)

The basic building blocks of many forms of optical topologies are particle-like singularities in phase and polarisation, giving rise to lines of darkness that weave complex threads in 3D space. Although known for half a century since seminal work on dislocations in wave trains, their behaviour in complex media remains under debate, especially with respect to their relative stability. Here we show that polarisation and phase vortices behave identically in one-sided turbulent complex channels. We perform complementary numerical and experimental studies using atmospheric turbulence as a test case, demonstrating agreement and equivalent dynamics. Our work addresses open questions on optical topologies and will be relevant to their harnessing for applications such as sensing, communication, imaging, and information transfer in noisy or complex environments.

Since the identification of wavefront dislocations by J. Nye and M. Berry [1], optical singularities have served as compact markers of field structure, capturing where a chosen field descriptor loses a unique definition [2]. In the scalar setting, an example is the optical vortex. It is defined as a point (or line) of vanishing complex amplitude around which the wavefront wraps, providing a natural route to beams carrying orbital angular momentum (OAM) [3]. Within this broader class of OAM states, the Laguerre-Gaussian (LG) modes occupy a particular position of interest. They provide a widely used modal basis whose azimuthal order sets a helical wavefront and radial order controls the ringed intensity profile, making them a standard platform for generating, combining, and diagnosing OAM content [4–6]. By arranging singularities through controlled superposition of such modes, one can assemble extended topological architectures, ranging from vortex lattices [7, 8] to knotted nodal filaments [9–11]. In vectorial fields, analogous design principles enable polarisation textures whose topology is encoded not only in the spatial distribution but also in how the local internal state is disposed across the beam cross-section [12–16].

A crucial separation must be drawn between phase singularities, known as defects of a complex scalar field that anchor OAM-carrying beams, and polarisation singularities, arising when the local polarisation state becomes indeterminate even though the total intensity may remain finite. Because these singularities reside in different field descriptors, the literature contains competing expectations of their resilience under external perturbations. One viewpoint emphasizes the quantized nature of the phase winding in OAM beams, arguing that the associated defect can shift or split but cannot be continuously eliminated, suggesting enhanced robustness to weak distortions [17, 18]. An opposing perspective notes that polarisation textures can persist when the channel primarily scrambles spatial modes while leaving the polarisation sector effectively coherent, so that vectorial structure can remain identifiable even as the scalar wavefront

becomes highly corrugated [19–21]. Therefore, reported conclusions depend sensitively on what quantity is used to define *stability*, which can be through the defect location [22, 23], OAM spectrum [24–26], or global topological descriptors [27, 28]. This ambiguity is particularly pronounced in atmospheric turbulence and other random environments, where the same disturbance can simultaneously broaden the OAM spectrum, induce vortex migration, and deform polarisation features, leading to a nontrivial comparison between phase- and polarisation-defined singular structures, often contradictory in some cases.

Here we address these contradictory perspectives by revealing the dynamics of both phase and polarisation singularities in one-sided complex channels, using atmospheric turbulence as an example. We outline theoretically how a one-sided channel acts on singularities in a manner that can be generalised to any degree of freedom. We confirm this experimentally by subjecting both phase and polarisation singularities to the same atmospheric turbulence conditions and quantify how the associated dislocation behaves in the far-field by inferring their wandering statistics and their sensitivity to increasing perturbation strength. This approach establishes an experimentally accessible benchmark for resolving prior ambiguities in comparative robustness and provides a concrete basis for designing structured-light encodings whose stability is set by the intended field descriptor.

To implement the phase-singular beam, we take a conventional scalar vortex beam given by a single Laguerre Gaussian (LG) mode with azimuthal index ℓ and zero radial order in a fixed polarisation state $\hat{\mathbf{e}}$, given by $\psi_{\text{ph}}(\mathbf{r}_{\perp}) = u_{\text{LG}}^{\ell}(\mathbf{r}_{\perp})\hat{\mathbf{e}}$, where the separability ensures that we have only a single spatial degree of freedom that can be acted on. For the polarisation-encoded dislocation, we define a two-component transverse field in the linear polarisation basis as a coherent superposition of a fundamental Gaussian mode ($\ell = 0$) in the horizontal channel $\hat{\mathbf{e}}_{\text{H}}$ and a single LG vortex mode in the vertical channel $\hat{\mathbf{e}}_{\text{V}}$, both evaluated at the same longitudinal plane $z = 0$

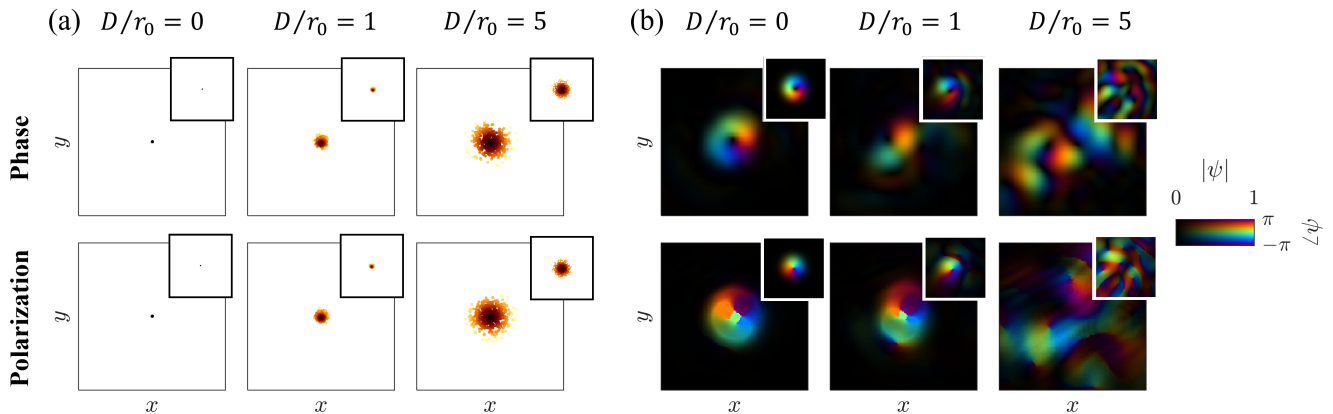


FIG. 1: (a) Singularity constellation distributions and (b) typical complex fields obtained for turbulent strengths $D/r_0 = 0, 1, 5$, respectively distributed across the rows. Within each panel, the top (bottom) row refers to the $\ell = 1$ vortex encoded in the phase (polarisation) distribution. Each inset refers to the simulation distributions, while the rest corresponds to their respective experimental result. The marker colours in panel (a) represent their respective distance from the constellation centroid. In panel (b), brightness represents the total amplitude $|\psi|$, while the colours refer to the phase $\angle\psi$ for the scalar vortex and to the Stokes field phase $\text{atan}(S_2/S_3)$ for the polarisation vortex.

across the transverse coordinates \mathbf{r}_\perp . In our notation, the polarisation-singular field is written compactly as

$$\psi_{\text{pol}}(\mathbf{r}_\perp) = u_{\text{LG}}^{\ell=0}(\mathbf{r}_\perp)\hat{\mathbf{e}}_H + u_{\text{LG}}^\ell(\mathbf{r}_\perp)\hat{\mathbf{e}}_V, \quad (1)$$

where u_{LG}^ℓ stands for the same LG mode previously defined. This field has two non-separable degrees of freedom (DoF) and ensures that the targeted singular behaviour is carried by the spatially varying inter-component phase relation rather than by the phase of a single scalar field, while keeping the modal content minimal and unambiguous. Now, both cases share the same OAM order but differ in whether the dislocation is encoded in a one-component phase structure or in a two-component polarisation superposition (polarisation singularity). The experimental setups used to generate both scalar and vector beams and simulate the effects of atmospheric turbulence are shown in the Supplementary Materials. The setups were carefully designed to ensure both singularity types were generated in a comparable manner and experienced identical realizations of the perturbing channel.

Suppose we wish to pass these two beams through a one-sided complex channel acting only on degree of freedom B while leaving the other (A) unaltered. In such a case the action of the channel is given by $\mathbb{1}_A \otimes T_B$, where $\mathbb{1}_B$ is the identity matrix and T_B is the channel operator. In what follows we will use atmospheric turbulence as our example so that the subscripts A, B refer to the polarisation and spatial DoFs respectively, but stress that these can be switched or altered to other DoFs for other complex channels. We select atmospheric turbulence as an exemplary one-sided channel (since it is

non-birefringent) because of its fundamental and practical importance. Such free-space channels often deteriorate the original transverse structure of light, as random refractive-index inhomogeneities imprint spatially varying optical-path delays, redistribute energy across the beam profile, and thereby perturb the dislocation geometry that carries the information or the topological descriptor. Here, the key question is not whether a singular pattern can be identified in an idealized field, but whether it remains traceable and statistically predictable after propagation through a stochastic medium, particularly when the singular structure is embedded either in a single-component wavefront or in a two-component polarisation superposition. To model atmospheric turbulence, we adopt the standard Kolmogorov description, which treats refractive-index fluctuations as a statistically homogeneous and isotropic random process with a scale-invariant cascade over an inertial range bounded by inner and outer lengths [29]. This framework relates turbulence strength and correlation scales to the induced wavefront distortions and intensity modulation, and forms the basis for the numerical phase-screen simulations used here. Details on the Kolmogorov model, turbulent phase screen generation, and experimental calibration are presented in the Supplementary Materials.

A direct way to compare the dynamical responses of the phase and polarisation vortices in turbulence is to quantify the wandering of their singularities, namely, the stochastic displacement of the defect coordinates across an ensemble of distorted realizations. Because the singularity position is a local observable that can be defined for both scalar and polarisation vortices, its statistics

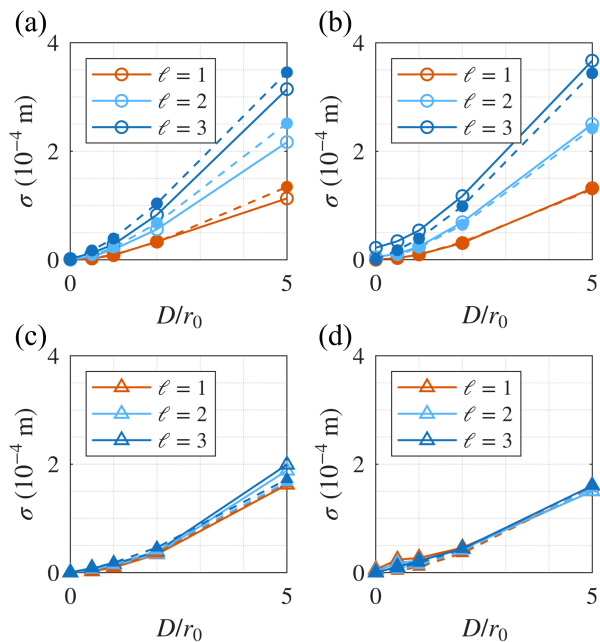


FIG. 2: Positional deviation radius σ as a function of the turbulence strength D/r_0 for (a) the phase singularity case and (b) the polarisation singularity case. The same experiment was repeated with corrected beam waists (see main text), (c) for the phase singularity case and (d) for the polarisation singularity case. All plots show the outcomes for topological charges $\ell = 1, 2, 3$, where the solid lines and hollow markers refer to the simulation results, while dashed lines and filled markers represent experiments.

provide a common metric for comparing the sensitivity of the corresponding topological descriptors to the same random medium. In practice, for each realization and both cases, we first determine the beam's centre of mass from the perturbed intensity distribution, which defines a robust reference point even when the pattern is distorted. For the $\ell = 1$ case, a single singularity is located close to the beam centre. For higher orders ($\ell = 2$ and $\ell = 3$), we identify $n = \ell$ singularities clustered around the centre-of-mass region, reflecting the expected local multiplicity near the beam core under perturbation. Aggregating these coordinates across all realizations yields a spatial occupancy map of singularity locations for each ℓ and each turbulence strength, parametrized by D/r_0 . Here, $D = 2w_0$ stands for the beam diameter with respect to its waist size, while r_0 refers to the Fried parameter. Throughout this work, a beam waist of $w_0 = 1$ mm was considered for both polarisation and phase vortices.

Figure 1 (a) shows a comparison between the typical constellation of singularity locations for $\ell = 1$ for the cases of both phase and polarisation vortices and turbu-

lence strengths $D/r_0 = 0, 1$, and 5 , respectively. Similarly, Fig. 1 (b) presents examples of the complex fields of scalar and vector beams obtained from simulations and experiments for $\ell = 1$ with the same turbulence strengths as in Fig. 1 (a). An ensemble of 500 realizations for each turbulence strength was used to obtain each constellation map, and details on the numerical simulations are provided in the Supplementary Materials. To further verify the similarities between the two cases observed in Fig. 1 (a), systematically compare wandering statistics across $\ell = 1, 2, 3$ for various turbulence levels by extracting their corresponding positional deviation radius $\sigma = \sqrt{\sigma_x^2 + \sigma_y^2}$, where $\sigma_{x,y}^2$ refers to the variance along the x, y directions. Across the full range of turbulence strengths explored, σ exhibits the same qualitative evolution for both types of vortices, as shown in Fig. 2 (a) and (b). Here, the distributions for phase and polarisation singularities, respectively, broaden monotonically with increasing D/r_0 , and, at a fixed turbulence level, the spread increases systematically as the topological charge changes from $\ell = 1$ to $\ell = 2$ and $\ell = 3$. This agreement shows that vortex wandering is set by turbulence-induced distortions, independent of whether the defect appears as a phase or polarisation vortex. Once the beam is referenced to its fluctuating centre of mass, the residual motion of the nearest singularity (or, for higher charge, the cluster of $n = \ell$ singularities) follows the same turbulence-driven statistics in both cases, leading to a comparable deviation scaling within the explored parameter space.

Generally, in a random but non-birefringent atmosphere, turbulence acts primarily as a polarisation-independent complex perturbation to the transverse field [30, 31]. Consequently, the polarisation component carrying the LG structure (in our case, vertical polarisation state) experiences essentially the same wavefront deterioration and transverse wavevector fluctuations whether it is analysed as a scalar field or embedded within a two-component polarisation superposition. The polarisation singularity is then bound to the evolution of that LG component, since the Gaussian mode counterpart serves mainly as a smooth reference, not introducing a competing singular structure. As a result, the singularity position extracted from the polarisation descriptor inherits the same random displacements as the underlying scalar LG vortex. This is established analytically in the Supplementary Materials. In a one-sided channel description, turbulence is modelled as a polarisation neutral transformation $\mathbb{1}_A \otimes T_B$, where $\mathbb{1}_B$ acting on the polarisation (A) and spatial (B) domains, which forces the phase vortex and the polarisation singularity tied to the same LG component to undergo identical transverse displacements. This can be shown explicitly for atmospheric turbulence using a wave-optics treatment, based on the Huygens-Fresnel propagation integral of a phase-distorted vectorial beam, which exhibits identical spatial

wandering of the two singularity types. The theoretical treatment is general, and is valid and can be adapted to a variety of systems ranging from non-unitary transformations to chiral media [32].

The systematic growth of total deviation radius σ with $|\ell|$ is likewise consistent with the greater susceptibility of higher-order vortices to random mixing into lower-order components. This is due to the instability of a multi-charge core, typically $|\ell| > 1$, which breaks into multiple unit-charge singularities whose relative positions are determined by the external perturbation [33, 34]. Both effects expand the ensemble of accessible singularity positions, producing broader constellation maps and consequently larger positional deviations for $|\ell| > 1$ in both scalar and polarisation vortex cases.

When the deviation analysis is repeated using corrected-scaling LG modes [35], implemented by adjusting the embedded beam waist as $w_0 \rightarrow w_0/\sqrt{|\ell|+1}$, the spatial deviation radius for $\ell = 1, 2, 3$ increases at nearly the same rate as the turbulence strength D/r_0 for both scalar and polarisation vortices. Figure 2 (c) and (d) shows the deviation curves as a function of the turbulence strength. This behaviour contrasts with the uncorrected case, where the apparent ℓ -dependence is amplified because higher-charge LG beams are typically larger and, therefore, sample a larger effective turbulence aperture. This result is consistent with prior observations that, once the beam size is decoupled from the topological charge, turbulence-induced OAM crosstalk becomes largely independent of the initial ℓ , as the relevant control parameter is the turbulence strength referenced to a common spatial scale rather than the charge itself. [36]. In our case, the same charge-independent broadening emerges in the positional statistics of the tracked singularities. As the LG-bearing component experiences the same polarisation-insensitive random phase perturbation in a non-birefringent channel, normalizing the mode size forces all ℓ modes to experience comparable distortions, and the resulting wandering deviation radius becomes approximately charge-invariant within experiments and simulation for both types of vortices.

To further condense the comparison into a single, vortex type-agnostic diagnostic, we directly plot the experimentally measured positional deviations σ for the polarisation-encoded singularities against the corresponding total deviation radius for the phase-encoded singularities, treating each turbulence condition and ℓ state as a point in a two-parameter space. In this representation, perfect equivalence corresponds to the identity line, and the fitted slope quantifies the relative response of the two vortex types to the same perturbations. Across the explored range of D/r_0 , the results follow a linear trend with slope near unity, indicating that the ensemble broadening of singularity positions is statistically equivalent in the two domains. Figure 3 summarizes these findings for both LG modes with uncorrected

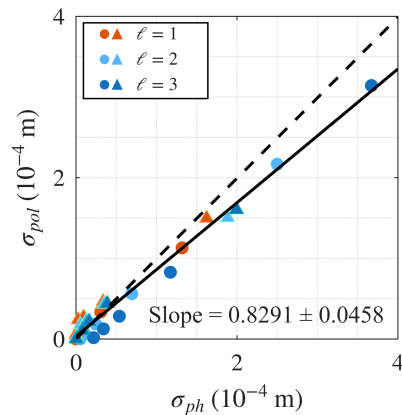


FIG. 3: Experimentally retrieved positional deviation radius for the polarisation (σ_{pol}) and phase (σ_{ph}) vortices generated using the LG mode with uncorrected (circles) and corrected (triangles) beam waist with topological charges $\ell = 1, 2, 3$. The black solid line refers to the experimental linear fit, with slope 0.8291 ± 0.0458 . The dashed line corresponds to the theoretical linear fit, with slope 0.9971 ± 0.0190 .

and corrected beam waists in experiments, with the inferred slope of 0.8291 ± 0.0458 in close agreement with theory which predicts a slope of 0.9971 ± 0.0190 . Deviations from theory primarily arise from finite ensemble size and experimental noise in singularity localization. Taken together, these results provide direct evidence of equivalent sensitivity to turbulence for phase and polarisation vortices.

In summary, we performed controlled experimental and numerical studies that place phase and polarisation singularities on equal footing through matched field generation, sampling, and intensity-referenced localization. Under identical turbulence conditions, the measured and simulated singularity constellation maps yield closely aligned positional deviation radii for scalar and polarisation vortices, demonstrating that the dominant wandering statistics are set by the turbulence acting on the shared structured component rather than by the vortex type. These results resolve longstanding ambiguity by identifying the conditions under which phase and polarisation singularities exhibit equivalent stability metrics. Our work provides a quantitative basis for selecting and normalizing structured light encodings for free-space optical links, turbulence-aware metrology, and environmental sensing where reliable singularity tracking, rather than ideal field reconstruction, is the operational figure of merit [37, 38].

* These authors contributed equally to this work.

† email:natalia.litchinitser@duke.edu

‡ email:andrew.forbes@wits.ac.za

- [1] J. F. Nye and M. V. Berry, Proceedings of the Royal Society of London. A. Mathematical and Physical Sciences **336**, 165 (1974).
- [2] M. Soskin and M. Vasnetsov, in *Progress in optics*, Vol. 42 (Elsevier, 2001) pp. 219–276.
- [3] S. Franke-Arnold, Nature Reviews Physics **4**, 361 (2022).
- [4] N. K. Fontaine, R. Ryf, H. Chen, D. T. Neilson, K. Kim, and J. Carpenter, Nature communications **10**, 1865 (2019).
- [5] C. Schulze, D. Naidoo, D. Flamm, O. A. Schmidt, A. Forbes, and M. Duparré, Optics express **20**, 19714 (2012).
- [6] M. Rafayelyan and E. Brasselet, Optics letters **42**, 1966 (2017).
- [7] L. Zhu, M. Tang, H. Li, Y. Tai, and X. Li, Nanophotonics **10**, 2487 (2021).
- [8] A. Dreischuh, S. Chervenkov, D. Neshev, G. G. Paulus, and H. Walther, Journal of the optical society of America B **19**, 550 (2002).
- [9] M. R. Dennis, R. P. King, B. Jack, K. O’holleran, and M. J. Padgett, Nature Physics **6**, 118 (2010).
- [10] J. Leach, M. R. Dennis, J. Courtial, and M. J. Padgett, New Journal of Physics **7**, 55 (2005).
- [11] D. Pires, D. Tsvetkov, H. Barati Sedeh, N. Chandra, and N. Litchinitser, Nature Communications **16**, 3001 (2025).
- [12] H. Larocque, D. Sugic, D. Mortimer, A. J. Taylor, R. Fickler, R. W. Boyd, M. R. Dennis, and E. Karimi, Nature Physics **14**, 1079 (2018).
- [13] Y. Shen, Q. Zhang, P. Shi, L. Du, X. Yuan, and A. V. Zayats, Nature Photonics **18**, 15 (2024).
- [14] Z. Guo, C. Peters, N. Mata-Cervera, A. N. Vetlugin, R. Guo, P. Zhang, A. Forbes, and Y. Shen, Nature Communications (2026).
- [15] X. Lei and Q. Zhan, Laser & Photonics Reviews , e01427 (2025).
- [16] D. G. Pires, J. Tan, H. B. Sedeh, and N. M. Litchinitser, Nanophotonics **14**, 4377 (2025).
- [17] I. Meglinski, I. Lopushenko, A. Sdobnov, and A. Bykov, Light: Science & Applications **13**, 214 (2024).
- [18] Z. Bouchal, Optics communications **210**, 155 (2002).
- [19] P. Lochab, P. Senthilkumaran, and K. Khare, Physical Review A **98**, 023831 (2018).
- [20] Y. Yu, M. Xu, M. Pu, J. Ding, S. Chen, Y. Zhang, S. Shi, Y. Guo, X. Li, X. Ma, *et al.*, Optics Letters **50**, 237 (2025).
- [21] P. Lochab, P. Senthilkumaran, and K. Khare, Applied Optics **58**, 6335 (2019).
- [22] Q. Cui, M. Li, and Z. Yu, Optics Communications **329**, 10 (2014).
- [23] Y. Gu, Journal of the Optical Society of America A **30**, 708 (2013).
- [24] M. P. Lavery, New Journal of Physics **20**, 043023 (2018).
- [25] S. Li and J. Wang, Optics letters **41**, 1482 (2016).
- [26] Y. Ren, G. Xie, H. Huang, C. Bao, Y. Yan, N. Ahmed, M. P. Lavery, B. I. Erkmen, S. Dolinar, M. Tur, *et al.*, Optics letters **39**, 2845 (2014).
- [27] A. A. Wang, Z. Zhao, Y. Ma, Y. Cai, R. Zhang, X. Shang, Y. Zhang, J. Qin, Z.-K. Pong, T. Marozsák, *et al.*, Light: Science & Applications **13**, 314 (2024).
- [28] C. Peters, M. Cox, A. Drozdov, and A. Forbes, Applied Physics Letters **123** (2023).
- [29] C. Peters, V. Cocotos, and A. Forbes, Advances in Optics and Photonics **17**, 113 (2025).
- [30] B. Ndagano, I. Nape, M. A. Cox, C. Rosales-Guzman, and A. Forbes, Journal of Lightwave Technology **36**, 292 (2017).
- [31] N. Cvijetic, D. Qian, J. Yu, Y.-K. Huang, and T. Wang, Journal of Lightwave Technology **28**, 1218 (2010).
- [32] I. Nape, K. Singh, A. Klug, W. Buono, C. Rosales-Guzman, A. McWilliam, S. Franke-Arnold, A. Kritzinger, P. Forbes, A. Dudley, *et al.*, Nature Photonics **16**, 538 (2022).
- [33] M. R. Dennis, K. O’holleran, and M. J. Padgett, in *Progress in optics*, Vol. 53 (Elsevier, 2009) pp. 293–363.
- [34] Y. Shen, X. Wang, Z. Xie, C. Min, X. Fu, Q. Liu, M. Gong, and X. Yuan, Light: Science & Applications **8**, 90 (2019).
- [35] V. Cocotos and A. Forbes, Journal of Optics **27**, 07LT01 (2025).
- [36] A. Klug, I. Nape, and A. Forbes, New Journal of Physics **23**, 093012 (2021).
- [37] Z. Chen, U. Daly, A. Boldin, and M. P. Lavery, Communications Physics **8**, 105 (2025).
- [38] M. Cheng, W. Jiang, L. Guo, J. Li, and A. Forbes, Light: Science & Applications **14**, 4 (2025).